Improving and fine-tuning the properties of peptide-based hydrogels via incorporation of peptide nucleic acids

Tristan Giraud, Sabine Bouguet-Bonnet, Philippe Marchal, Guillaume Pickaert, Marie-Christine Averlant-Petit, Loïc Stefan

To cite this version:

Tristan Giraud, Sabine Bouguet-Bonnet, Philippe Marchal, Guillaume Pickaert, Marie-Christine Averlant-Petit, et al.. Improving and fine-tuning the properties of peptide-based hydrogels via incorporation of peptide nucleic acids. Nanoscale, 2020, 12 (38), pp.19905-19917. ⟨10.1039/D0NR03483E⟩. ⟨hal-02996576⟩

HAL Id: hal-02996576
https://hal.science/hal-02996576v1

Submitted on 9 Nov 2020

Nanoscale

PAPER

Cite this: DOI: 10.1039/d0nr03483e

Improving and fine-tuning the properties of peptide-based hydrogels *via* incorporation of peptide nucleic acids†

Q2 Tristan Giraud,[a] Sabine Bouguet-Bonnet,[b] Philippe Marchal,[c] Guillaume Pickaert,[a] Marie-Christine Averlant-Petit[a] and Loic Stefan *[a]

Peptide self-assemblies have attracted intense research interest over the last few decades thanks to their implications in key biological processes (*e.g.*, amyloid formation) and their use in biotechnological and (bio)material fields. In particular, peptide-based hydrogels have been highly considered as high potential supramolecular materials in the biomedical domain and open new horizons in terms of applications. To further understand their self-assembly mechanisms and to optimize their properties, several strategies have been proposed with the modification of the constituting amino acid chains *via*, *per se*, the introduction of D-amino acids, halogenated amino acids, pseudopeptide bonds, or other chemical moieties. In this context, we report herein on the incorporation of DNA-nucleobases into their peptide nucleic acid (PNA) forms to develop a new series of hybrid nucleopeptides. Thus, depending of the nature of the nucleobase (*i.e.*, thymine, cytosine, adenine or guanine), the physicochemical and mechanical properties of the resulting hydrogels can be significantly improved and fine-tuned with, for instance, drastic enhancements of both the gel stiffness (up to 70-fold) and the gel resistance to external stress (up to 40-fold), and the generation of both thermo-reversible and uncommon red-edge excitation shift (REES) properties. To decipher the actual role of each PNA moiety in the self-assembly processes, the induced modifications from the molecular to the macroscopic scales are studied thanks to the multiscale approach based on a large panel of analytical techniques (*i.e.*, rheology, NMR relaxometry, TEM, thioflavin T assays, FTIR, CD, fluorescence, NMR chemical shift index). Thus, such a strategy provides new opportunities to adapt and fit hydrogel properties to the intended ones and pushes back the limits of supramolecular materials.

Received 4th May 2020,
Accepted 4th August 2020

DOI: 10.1039/d0nr03483e

rsc.li/nanoscale

Introduction

Q4 Owing to their pivotal roles in biological systems, protein and peptide self-assemblies are involved in the formation of a wide variety of three-dimensional structures, from filaments to rings, tubes, catenanes, knots or cages.[1,2] Although protein self-assemblies are crucial for many physiological processes (*e.g.*, proteasomes for enzymatic reactions, G-proteins for signal transduction, hemoglobin A for oxygen transport) and as structural elements (*e.g.*, collagen, keratin, and elastin), they are also related to several pathologies, including neurodegenerative (*e.g.*, Parkinson's and Alzheimer's diseases and amyotrophic lateral sclerosis)[3] and cataract diseases[4,5] with the formation of amyloid fibrils, or sickle cell anemia due to hemoglobin tetramer assemblies.[6] The ability of proteins to form highly ordered architectures has been harnessed by the scientific community to develop controlled supramolecular objects such as nanowires, nanotubes, two-dimensional lattices, or icosahedral three-dimensional cages to name a few, with applications in biomedicine, nanotechnology or materials science.[7–9]

Being shorter than proteins, peptides have also been extensively studied and preferred thanks to their easier access and lower cost in peptide synthesis, and an easier control of their structuration compared to proteins. Thus, designed peptides can self-assemble into a myriad of complex tridimensional structures from nanotubes to nanovesicles, nanofibers, nanospheres, nanodoughnuts, nanorods or micelles (*e.g.*, spherical, cylindrical or worm-like) to name a few.[10] All these assemblies rely on non-covalent interactions between peptide units which self-organize adopting mainly α-helix, β-sheet or β-turn secondary structures.[11] They have an ever-increasing number of applications as confirmed by the use of peptide-self-assemblies in the fields of energy storage, display and light emitting devices,

---

Q3 [a] *Université de Lorraine, CNRS, LCPM, F-54000 Nancy, France*
[b] *Université de Lorraine, CNRS, CRM2, F-54000 Nancy, France*
[c] *Université de Lorraine, CNRS, LRGP, F-54000 Nancy, France*

† Electronic supplementary information (ESI) available. See DOI: 10.1039/d0nr03483e

piezoelectric components, sensors, therapeutics and biomaterials.[12] In the latter case, peptide hydrogels have been attracting intense research interest over the last twenty years thanks to, *per se*, their ability to mimic the extracellular matrix.[13,14] Far from being only lab curiosity, peptide hydrogels have come into prominence as evidenced by the recent launches of commercially available products (*e.g.*, PuraMatrix®, Hydromatrix®, and PeptiGel®) mainly sold as matrices for stem cell culture.[15]

Along with proteins and peptides, DNA and RNA are the other major classes of biomolecules exhibiting high self-assembly potential. Owing to their pivotal biological roles in the genome, transcriptome and gene regulation, they can adopt a wide variety of tridimensional structures from the iconic canonical right-handed anti-parallel DNA duplex to diverse duplex forms, triplexes, i-motifs and G-quadruplexes.[16,17] This high polymorphism originates from the versatility of interactions nucleobases (*i.e.*, adenine, thymine/uracil, guanine and cytosine) can make, mainly based on hydrogen bonds and π-stacking interactions. Such properties have inspired chemists, who have seized the nucleobase moieties to create a large panel of (nano)technological systems, with the development of nanoparticles, catalysts, nanomaterials, biosensors, membranes, nucleogels, nanocarriers or DNA origami just to cite a few examples.[18–21]

Thanks to the outstanding self-assembly qualities of each system (i.e., proteins/peptides on the one side and nucleobases on the other), their combination has a tremendous opportunity to construct new complex supramolecular architectures providing new functions and properties. Nature exploits these protein and nucleobase assemblies with (ribo)nucleoproteins interacting with RNA or DNA in a non-covalent (e.g., histones, telomerase, ribosome)[22,23] or, more rarely, covalent (e.g., topoisomerase I, Ku protein)[24–26] way. Not surprisingly, artificial protein–nucleobase architectures have been developed over the last few decades and used to design controlled nanoobjects including nanoarrays, nanowires, nanotubes, linear and branched nanostructures or superlattices, and both their conception and study remain challenging.[27] Being shorter than proteins, peptides functionalized with nucleobases are emerging in the nanotechnological field and have been harnessed to form precisely controlled nanofibers, nanorods, toroidal and multilamellar spherical structures or hollow spherical structures.[28] Besides their impact on the assembly process, nucleobases have been reported to bring additional properties to the materials, such as fluorescence[29] and non-reversible or reversible reorganization of the fibrillar structure upon addition of DNase[30] or ATP/ADP,[31] respectively. Interestingly, the incorporation of nucleobases into peptide sequences to develop new macroscopic materials (e.g., hydrogels and organogels) has only been recently considered and remains highly limited with only a dozen of published works.[28] Among them, the Xu group reported on the first peptide/nucleobase hybrids built on the highly hydrophobic PhePhe and PhePheTyr peptide sequences.[32] The nature of the nucleobase grafted on the N-term as a carboxylic acid derivative clearly impacts the mechanical and structural properties of the gels. They have subsequently developed new systems with nucleobases grafted on lysine (N-ε position),[33] with complementary peptide sequences,[34] with the incorporation of glycoside moieties,[35,36] or exhibiting sensitivity to ATP addition.[31] Using a multicomponent approach, the Nilsson group has described a complex system composed of three peptides (i.e., one native, the two others being functionalized with distinct 10-mer nucleic acids) and an extra single-stranded DNA to improve fibril–fibril crosslinking.[37] Even if not fully understood, this proof of concept has opened the way to new strategies for peptide fibril hybridization. Indeed, one year later, the Stupp group reported on a responsive hydrogel based on nanopeptides bearing complementary nucleotide sequences.[38] Once mixed, the peptide parts co-assemble into fibers, crosslinked with double helix formation thanks to complementary base pairing, modifying the mechanical and structural properties of the gels. All these examples highlight the interest and the high potential of peptide–nucleobase hybrids as innovative hydrogelators. To understand and decipher the parameters influencing their assembly processes, further investigations using a multi-scale approach are essential and will constitute a solid basis to expand the scope of application of promising nucleobase–peptide hybrid systems.

In this context, we report on the impact of peptide nucleic acid (PNA) moieties as an efficient modification to improve and fine-tune peptide-based hydrogel properties, thanks to the multiscale approach. Starting from a reference charged octapeptide, we studied the assembly abilities of four different peptide–PNA hybrids on the mechanical properties, thermoreversibility, kinetics of both gel and fibril formation, fibril morphologies, supramolecular organization, and fluorescence properties.

Results and discussion

Although nucleobases have been introduced into peptide sequences as it (*i.e.*, *via* a carboxylic acid arm[34] requiring multi-step organic synthesis) or as its nucleoside[39] or nucleotide forms, we chose their peptide nucleic acid (PNA) forms in this study. Mainly used for biological applications, PNA are good alternatives to DNA in material science, thanks to their better chemical stability, the reduction of non-specific electrostatic repulsions (due to the absence of charge) and the more stable duplexes they form.[40,41] Owing to their shorter length than the well-known RADA-16 and MAX peptide derivatives,[11] we selected the octapeptide Phe-Glu-Phe-Glu-Phe-Lys-Phe-Lys (without any protection at the N- and C-termini, alternating charged and aromatic amino acids and first reported at the end of the 2000s by the Saiani group)[42,43] as our reference compound (termed **N-pep** herein). Thanks to its ability to form hydrogels at neutral pH, this peptide has found applications in biomedical and biotechnological contexts, including as drug delivery vehicles[44] and as cell culture scaffolds for cell encapsulation,[45] for intervertebral disc tissue engineering[46] and for osteogenic differentiation of stem cells both *in vitro*[47] and *in vivo*.[48] Thus, six peptide derivatives, depicted in Fig. 1,

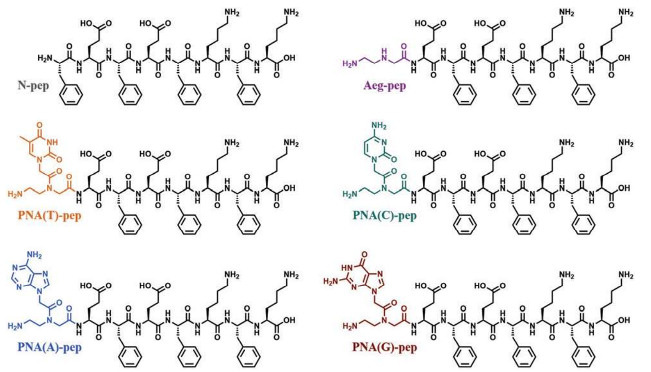

Fig. 1 Chemical structures of the native octapeptide **N-pep**, the control compound **Aeg-pep** and the four nucleopeptides **PNA(X)-pep** with X = **T**, **C**, **A**, and **G**.

are considered in this study: **PNA(A)-pep**, **PNA(T)-pep**, **PNA(C)-pep**, and **PNA(G)-pep** in which a PNA moiety substitutes the last phenylalanine in order to keep the same length as that of the native peptide **N-pep**, and **Aeg-pep** (with *Aeg* corresponding to the *N*-(2-aminoethyl) glycine moiety). The latter is our second reference to evaluate the impact of the "PNA arm" without the presence of a nucleobase.

All the compounds were synthesized at a 400 μmol-scale by solid-phase peptide synthesis with a Fmoc/^{t}Bu strategy. Briefly, each amino acid was introduced *via* a double coupling using 6 equiv. Fmoc-amino acid, 5 equiv. HBTU and 10 equiv. NMM in DMF and NMP with a 40 min coupling time, except for the N-term PNA and Aeg moieties introduced manually using 4 equiv. Fmoc-PNA/Fmoc-Aeg derivative, 3.5 equiv. HBTU and 7.5 equiv. NMM in DMF and NMP (double coupling, 3 hours). The peptides and nucleopeptides were subsequently purified by reverse-phase HPLC, fully characterized by LC-MS, ESI-HRMS, ^{1}H, ^{13}C and 2D NMR (COSY, NOESY, ROESY, and TOCSY in DMSO-d_6, 5 mM) and obtained with 50.3% to 62.2% yield (see the ESI† for more details on synthesis and chemical characterization). While PNA are achiral moieties,[40,41] we noticed a splitting of the proton signals corresponding to the three contiguous amino acids (*i.e.*, Glu, Phe and Glu, see the ESI†) due to the two conformations adopted by the tertiary amine on the *N*-(2-aminoethyl) glycine moiety.

Using the so-called tube inversion test[49] as preliminary assays, we first investigated the ability of all the compounds to form hydrogels in a wide range of pH values (from 2 to 12, Fig. S1 and Table S1†). Although translucent gels were obtained with the octapeptide **N-pep** only at highly acidic pH 2–3 and from neutral to basic pH, the incorporation of PNA moieties allows the formation of hydrogels at all acidic pH and, especially for **PNA(A)-pep** and **PNA(G)-pep**, up to pH 11, improving the operating window. Subsequently, pH 7.4 (buffer Tris·HCl, 1 M) was chosen as our standard biologically relevant conditions with which homogeneous and self-supporting hydrogels are obtained in a reasonable amount of time (<6 hours) for all the compounds. The concentration of 15 mM was also selected according to the already reported peptide-based hydrogels,[50–54] allowing a direct comparison of the properties between different systems. To assess the viscoelastic properties of all the hydrogels, time-dependent rheological measurements were carried out using a Couette geometry immersed in the sample (Fig. S3†). As observed in Fig. 2a (and Fig. S4†), the gelification process is triggered instantly after mixing without induction time, and all the soft materials exhibit distinct mechanical properties characterized by their storage modulus (G') and loss modulus (G''). After 6 hours, while the reference peptide **N-pep** forms a gel with a G' value of 320 Pa,[55] the substitution of its N-term phenylalanine by a *N*-(2-aminoethyl) glycine moiety only slightly reduced this value to 191 Pa, indicating that the loss of an aromatic group is not detrimental to the gelification process (Fig. 2b). The impact of the nucleobases on the mechanical stiffness can be divided into two groups: on the one hand, the presence of pyrimidines (*i.e.*, thymine and cytosine) does not significantly modulate the storage moduli with G' = 319 Pa and 201 Pa for **PNA(T)-pep** and **PNA(C)-pep**, respectively. On the other hand, nucleopeptides containing a purine (*i.e.*, adenine or guanine) lead to a drastic improvement in the mechanical properties of the resulting hydrogels of 20-fold and 70-fold for **PNA(A)-pep** (G' = 6512 Pa) and **PNA(G)-pep** (G' = 21 650 Pa), respectively (Fig. 2b). After a longer period of time (up to eight days, Fig. S5 and Table S2†), while the mechanical properties of **Aeg-pep** and **N-pep** collapse, **PNA(A)-pep** and **PNA(G)-pep** are quite stable, unlike **PNA(C)-pep** and **PNA(T)-pep** which are still evolving, highlighting a very slow kinetics of formation for the latter two. With a storage modulus higher than 20 kPa at 15 mM after 6 h (and up to 40.3 kPa after 8 days, see Table S2†), **PNA(G)-pep** is among the most efficient peptide-based hydrogels reported so far, including the octapeptide Ac-GLYGGYGV-NH_2 ($G' \approx 5$ kPa at 15 mM),[53] the pentapeptide DF

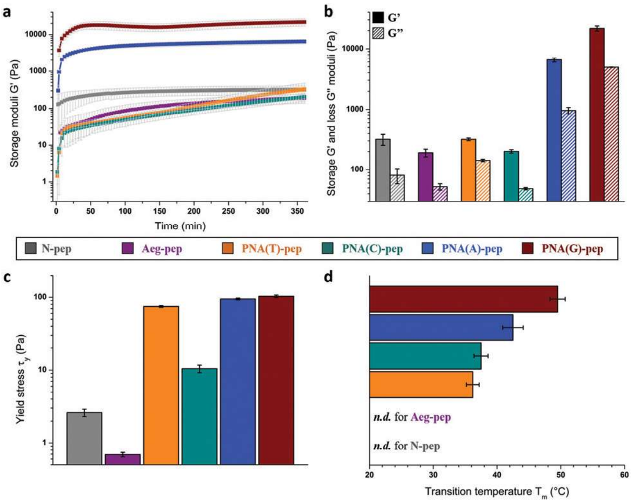

Fig. 2 (a) Time sweep rheological profiles and (b) plot of the resulting storage (G') and loss (G'') moduli after 6 hours (20 °C). Plot of the characteristic (c) limiting values of the linear viscoelastic region (at 20 °C) and (d) transition temperatures determined by rheology. All the experiments were carried out at 15 mM sample in Tris·HCl (1 M, pH 7.4).

(I)NKF(I) ($G' \approx 20$ kPa at 15 mM, F(I) for *para*-iodinated phenylalanine),[50] the hexapeptide Ac-LIVAGD-NH_2 ($G' \approx 25$ kPa at 12 mM)[56] and its derivative Ac-ILVAGK-NH_2 ($G' \approx 18$ kPa at 15.6 mM).[54] To determine the deformation behavior of all these hydrogels, stress sweep experiments (with controlled shear strain) were subsequently carried out (Fig. S6†) and the limiting values of the linear viscoelastic region (*i.e.*, the yield point τ_y) beyond which the structure of the gel is destroyed are plotted as shown in Fig. 2c. Although the reference peptides **N-pep** and **Aeg-pep** have low stress resistance (τ_y = 2.6 Pa and 0.7 Pa, respectively), the presence of one nucleobase significantly improves the yield point from 10.4 Pa for **PNA(C)-pep** to 74.7 Pa, 94.7 Pa and 103 Pa for **PNA(T)-pep**, **PNA(A)-pep** and **PNA(G)-pep**, respectively (*i.e.*, an improvement in the resistance to external stress of up to 40-fold compared to **N-pep**). After applying high stress beyond the yield point τ_y to break the gel, we measured the ability of all hydrogels to recover their initial mechanical properties. The rheological data (Fig. S7 and S8†) highlight the thixotropic behaviors[57] of **PNA(T)-pep** and **PNA(C)-pep**, whereas for **PNA(A)-pep** and **PNA(G)-pep** a loss of mechanical properties happens, mainly after the first break. The thermal behaviors of all the hydrogels, visually observed in the preliminary assays, are also influenced by the nucleobases. Indeed, all four nucleopeptides **PNA(X)-pep** (**X** = **T**, **C**, **A**, and **G**) exhibit a gel-to-sol transition, characterized by the transition temperatures T_m ranging between 36.2 °C and 49.5 °C (Fig. 2d, Fig. S9 and Table S3†), contrasting with **N-pep** and **Aeg-pep** for which no significant storage and loss moduli variations were observed from 20 °C to 90 °C. The pyrimidine-containing compounds show lower values than the purine-containing ones, with T_m = 36.2 °C and 37.5 °C for **PNA(T)-pep** and **PNA(C)-pep**, respectively, and T_m = 42.5 °C and 49.5 °C for **PNA(A)-pep** and **PNA(G)-pep**, respectively (Fig. 2d and Table S3†). To assess the potential of all the compounds for biomedical and biotechnological applications such as in tridimensional cell culture scaffolds, drug delivery, tissue engineering or bioprinting,[14,58] the mechanical properties were evaluated at physiological temperature (*i.e.*, at 37 °C). Under these conditions, although **N-pep** and **Aeg-pep** form weak gels with $G' < 120$ Pa, **PNA(T)-pep** and **PNA(C)-pep** are viscous liquids since there are both close to their transition temperature T_m (Table S3†). In contrast, **PNA(A)-pep** and **PNA(G)-pep** are stable hydrogels at 37 °C, exhibiting medium (481 Pa) and high (6509 Pa) storage moduli (Table S3†), respectively, and are consequently perfectly suitable for biomedical applications. On exploring the thermal behaviors of the hydrogels, we observed that, once heated at high temperature (85 °C), all the **PNA(X)-pep**-based hydrogels recovered their initial mechanical properties after cooling to 20 °C. Thus, such a heating/cooling sequence was applied several times to each gel, and the results (Fig. 3 and Fig. S10†) highlight that the presence of a nucleobase induces thermo-reversibility without loss of mechanical properties (G'/G'' ratio remains similar after numerous heating/cooling cycles), a property reported predominantly for polymers[59] and composite hydrogels, but scarcely for peptide derivatives.[58,60] All these rheological data attest the positive impacts of nucleobases on the macroscopic properties of the formulated gels.

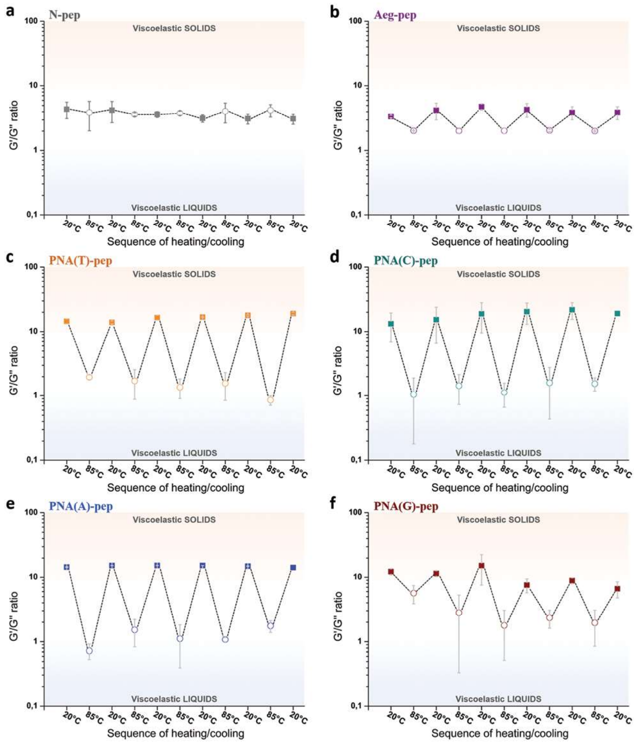

Fig. 3 Thermal recovery behavior of the hydrogels (15 mM in Tris·HCl (1 M, pH 7.4)) during cycles of heating/cooling. From the starting G'/G'' ratio, characteristic of the mechanical properties of each hydrogel, a decrease of this value is indicative of fluidification (gel-to-sol transition) of the gel, while a subsequent increase exhibits the re-gelification of the sample.

Q8

Before focusing our attention on the peptide and nucleopeptide self-assemblies *per se*, we first studied the behavior of the main constituent of the soft material, *i.e.*, water (>98 weight%), using NMR relaxometry.[61,62] In this study (Fig. 4a), the longitudinal relaxation rates (inverse of longitudinal relaxation times $R_1 = 1/T_1$) of solvent's protons were plotted as a function of Larmor frequency (from 50 kHz to 10 MHz), and the deconvolution of the curves *via* Lorentzian fittings reveals the presence of two main water populations for the nucleopeptide derivatives (*nota bene*: no reliable fits were obtained for **N-pep** and **Aeg-pep** because their relaxation profiles are too broad and too weak, respectively). The first population, observed at low frequencies, corresponds to constrained water identified as confined water molecules in direct interaction with the peptide scaffold, exhibiting a similar slow movement in all the nucleopeptide-based hydrogels with a correlation time $\tau_c(2) = {\sim}7 \times 10^{-6}$ s. By contrast, the second population of more free water is observed at higher frequencies, with characteristic correlation times higher for **PNA(G)-pep** and **PNA(A)-pep** ($\tau_c(1) = 151 \times 10^{-9}$ s and 109×10^{-9} s, respectively) than for **PNA(C)-pep** and **PNA(T)-pep** ($\tau_c(1) = 94 \times 10^{-7}$ s and 55×10^{-7} s, respectively) based hydrogels, indicating a more constrained

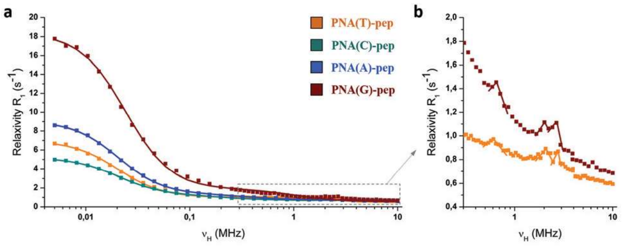

c	PNA(T)-pep	PNA(C)-pep	PNA(A)-pep	PNA(G)-pep
A(0) (s^{-1})	0.54	0.54	0.54	0.54
A(1) (s^{-1})	0.42	0.42	0.59	1.33
τ_c**(1)** (s)	55 x10^{-9}	94 x10^{-9}	109 x10^{-9}	151 x10^{-9}
A(2) (s^{-1})	6.00	4.14	7.86	16.49
τ_c**(2)** (s)	7.8 x10^{-6}	6.8 x10^{-6}	7.4 x10^{-6}	6.6 x10^{-6}
$r_1 = \frac{A(1)}{\tau_c(1)}$ (s^{-2})	7.65 x10^{6}	4.42 x10^{6}	5.44 x10^{6}	8.81 x10^{6}
$r_2 = \frac{A(2)}{\tau_c(2)}$ (s^{-2})	0.77 x10^{6}	0.61 x10^{6}	1.06 x10^{6}	2.48 x10^{6}
$\frac{r_2}{r_2+r_1}$	9	12	16	22

Fig. 4 (a) ^{1}H NMRD profiles (longitudinal relaxation rate R_1 in s^{-1} as a function of the Larmor frequency ν_H in MHz) measured on **PNA(T)-pep**, **PNA(C)-pep**, **PNA(A)-pep** and **PNA(G)-pep**. Continuous lines represent the best fits obtained with a sum of lorentzian functions: $R_1(\nu_H) = A(0) + \sum_i \frac{A(i)}{1+(2\pi\nu_H\tau_c(i))^2}$ where τ_c is the correlation time describing the water motion (see numeric values in (c). The proportion of water experiencing very slow motion (last row in (c)) was obtained by comparing the weight of the lorentzian functions ($r_i = A(i)/t_c(i)$) in each sample. (b) Enlargement of the NMRD profiles in the 0.3–10 MHz Larmor frequency range, showing the presence of quadrupolar peaks at 0.6, 2.0 and 2.7 MHz in the **PNA(T)-pep** and **PNA(G)-pep** samples.

water in the purine (**G** and **A**) than in the pyrimidine (**C** and **T**) derivatives. The comparison of the two water population ratios (obtained in comparing the weight of each lorentzian, corresponding to the two motions) clearly highlights a higher proportion of restricted water molecules in interaction with the peptide network for **PNA(G)-pep** > **PNA(A)-pep** > **PNA(C)-pep** > **PNA(T)-pep** (values $r_2/(r_1 + r_2)$, Fig. 4c). These data can be correlated with smaller pore size for the guanine derivative than for the others. The hierarchy observed in NMR relaxometry is in accordance with the rheological data discussed (*vide supra*) in which stiffer hydrogels were obtained for purine than for pyrimidine-containing nucleopeptides, even if the cytosine and thymine-based compounds are inverted, explained by other factors, including the formation of other objects at the nanoscale (discussed later). Interestingly, at 0.6, 2.0 and 2.7 MHz, **PNA(G)-pep** and **PNA(T)-pep** exhibit quadrupolar peaks (Fig. 4b), attributed to the imino and the imido groups on the guanine and thymine moieties, respectively. Indeed, quadrupolar peaks originate from dipole–dipole interactions between a dipolar nucleus of the spin quantum number $\frac{1}{2}$ (^{1}H here) and a neighboring quadrupolar nucleus of the spin quantum number ≥1 (^{14}N here, $I = 1$), corresponding, in our case, to the N–H.[63–65] Although the tertiary amines of adenine and cytosine are too labile, the exchangeable N–H protons of guanine and thymine induce quadrupolar peaks in water NMRD profiles because the mobility of these moieties was slowed down. This indicates that the nucleobases are in a blocked conformation inside the gel and that their N–H protons are not engaged by hydrogen bonds. These results show that the nucleobases are involved in the formation of the hydrogel structure, *i.e.*, in the self-assembly of the compounds into nanostructured architectures.

To assess the scaffold morphology of the hydrogels and the nanostructures of peptide and nucleopeptide self-assemblies, transmission electron microscopy (TEM) was performed on all the samples (Fig. 5). The native peptide **N-pep** revealed its ability to self-organize into entangled long fibers (>1 µm) with diameters of 30.5 ± 4.5 nm inducing large pore size, contrasting with **Aeg-pep** in which disparate 10 nm to ~500 nm-long fibers with shorter diameters (*i.e.*, 12.3 ± 2.3 nm) were observed. The low fiber density of the latter explains its low mechanical properties determined by rheology and the low water dispersity in NMR relaxometry (*vide supra*). However, for all the nucleopeptides **PNA(X)-pep** (**X** = **T**, **C**, **A**, and **G**), very dense deposits of entangled fibers were imaged, and the longest and biggest ones were obtained for guanine (diameter 5.1 ± 0.2 nm, >1 µm-long) and adenine (diameter 4.9 ± 0.6 nm, >100 nm-long) derivatives. Compared to **N-pep**, the increased number of entanglements induces higher stiffness and better mechanical stress resistances for **PNA(G)-pep** and **PNA(A)-pep**, as well as a lower porosity, confirmed by more constrained

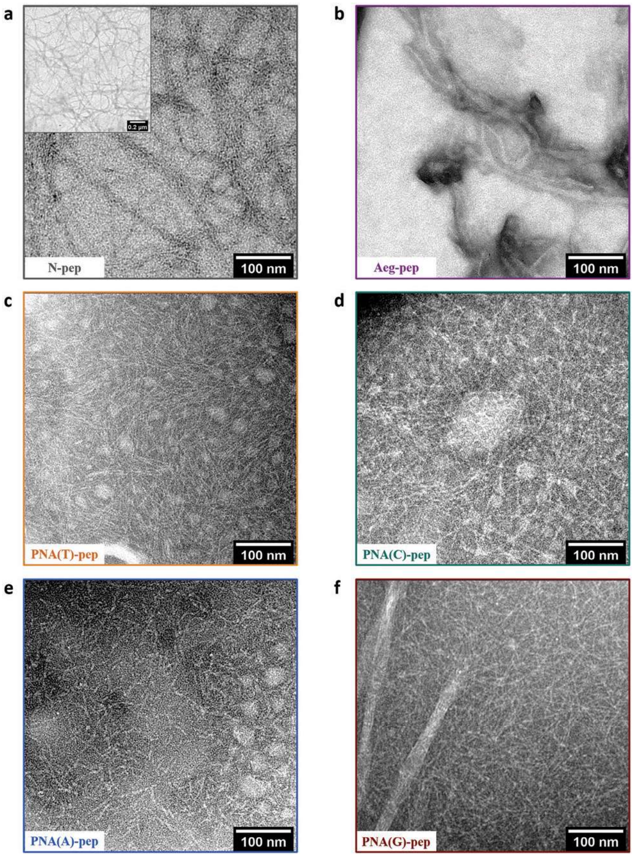

Fig. 5 TEM images of all the nucleopeptides recorded with a magnification of ×38 000 (inserted image for **N-pep** ×6600) and negative staining by phosphotungstic acid.

water molecules observed in relaxometry (*vide supra*). We assume that such morphological differences explain, partially, the thermo-reversible properties: upon heating, thinner nanostructures are more prone to disassemble to regenerate the starting monomeric nucleopeptides (leading to a gel-to-sol transition), while larger fibers (*i.e.*, **N-pep**) are, *per se*, more stable supramolecular structures (leading to a gel state in a broader range of temperatures). For **PNA(G)-pep** and **PNA(A)-pep**, the coalescence of fibers also leads to the formation of higher-ordered nanostructures defined as fibril bundles of 28.4 ± 1.6 nm and 44.0 ± 1.7 nm-cross-section, respectively. The TEM images of the two pyrimidine-containing nucleopeptides also show dense networks of thin fibers (diameters 4.6 ± 0.4 nm and 2.5 ± 0.3 nm for **PNA(C)-pep** and **PNA(T)-pep**, respectively), in which additional spherical nanostructures with a uniform size distribution of around 25 nm are observed, as already reported for other peptide self-assemblies.[66,67] It should be noted that **PNA(C)-pep** also forms bigger heterogeneous 100–250 nm aggregates covered by a fibril-like material[68,69] (Fig. 5d and Fig. S11†). These morphological differences support the mechanical behaviors determined by rheology: although the overwhelming majority of peptide-based hydrogels are composed of fibrillar structures,[11] the presence of spherical aggregates in **PNA(C)-pep** and **PNA(T)-pep** hydrogels weakens the hydrogel properties as previously described.[70]

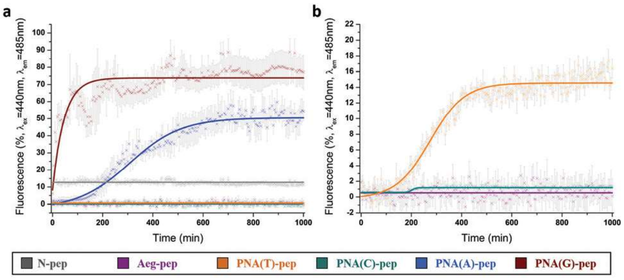

c	N-pep	Aeg-pep	PNA(T)-pep	PNA(C)-pep	PNA(A)-pep	PNA(G)-pep
Max. intensity (a.u.)	**12.74** (dev. std. 1.04)	**0.52** (dev. std. 1.89)	**17.05** (dev. std. 1.14)	**1.18** (dev. std. 0.25)	**50.30** (dev. std. 4.82)	**73.8** (dev. std. 9.36)
$\mathbf{t_{lag}}$ (min)	**< 1**	*n.d.*	**87.9** (dev. std. 5.4)	**178.9** (dev. std. 1.1)	**75.0** (dev. std. 6.0)	**< 1**
$\mathbf{k_{app}}$ (h^{-1})	*n.d.*	*n.d.*	**3.13** (dev. std. 0.13)	**1.00** (dev. std. 0.12)	**7.78** (dev. std. 0.55)	**64.58** (dev. std. 3.62)

Fig. 6 (a) Fibril formation monitored by thioflavin T fluorescence (λ_{ex} = 440 nm and λ_{em} = 485 nm) assay as a function of time (PMT detector sensitivity = 800 V). (b) To improve the fluorescence signal of **Aeg-pep**, **PNA(C)-pep** and **PNA(T)-pep**, the same experiments were carried out at higher sensitivity (PMT = 1000 V). (c) Characteristic maximum intensities, lag time (t_{lag}) and apparent rate constants (k_{app}) reported for all the samples. All the experiments were carried out at 5 mM sample in Tris·HCl (1 M, pH 7.4) at 25 °C.

To assess the morphological and kinetic parameters of the fiber formation, thioflavin T (also termed ThT) assay, a fluorescent test widely used to diagnose amyloid fibrils involved in several human pathologies (*e.g.*, Parkinson's, Alzheimer's and Prion's diseases)[71,72] was carried out. When free in solution, ThT is not fluorescent and becomes fluorescent (λ_{ex} = 450 nm and λ_{em} = 485 nm) upon perpendicular binding to the β-strands in the β-sheets (*i.e.*, parallel to the long axis of the fibril). Often restricted to a "on/off" probe in peptide-based material studies,[73,74] the variation of ThT fluorescence as a function of time gives invaluable information on the peptide/nucleopeptide self-assemblies. As depicted in Fig. 6, the maximum fluorescence intensities were obtained at the final plateau for **PNA(G)-pep** and **PNA(A)-pep** with I = 73.8% and 50.3%, respectively, far higher than the other compounds. These maximum intensities, linked to the fibril numbers and morphologies,[71,72] are consistent with the TEM images (less fibers were observed for **PNA(C)-pep** and **PNA(T)-pep** due to the formation of spherical nano-objects) and are in perfect accordance with the hierarchy observed in rheology and relaxometry: the more intense the signal, the stiffer the gel and the more constrained the water molecules (*vide supra*). In terms of kinetics, the lag times t_{lag} (Fig. 6c), defined as the end of the non-fluorescent initial state in which starting monomers undergo primary nucleation, still follow the same tendency discussed above, with **PNA(G)-pep** (t_{lag} < 1 min) < **PNA(A)-pep** (t_{lag} = 75 min) < **PNA(T)-pep** (t_{lag} = 88 min) < **PNA(C)-pep** (t_{lag} = 179 min). After the lag time, the very short fragments of fibrils start to grow, inducing a steep increase in fluorescence (termed the growth phase), characterized by an apparent rate constant k_{app}. Once again, **PNA(G)-pep** exhibits the faster fibril elongation, outstripping **PNA(A)-pep** with k_{app} = 64.6 h^{-1} and 7.8 h^{-1}, respectively, far better than **PNA(T)-pep** and the slowest **PNA(C)-pep** (k_{app} = 3.1 h^{-1} and 1.0 h^{-1}, respectively, Fig. 6c). Although not a general rule,[75,76] we observe that the faster the kinetics of formation, the stiffer the gel, as already reported.[60,77] Thus, the nature of the nucleobase impacts both the kinetics of formation and the morphology of the fibres, modulating the mechanical properties of the resulting hydrogels.

Thanks to the specific binding mode of ThT and the TEM images, it is safe to assume that nucleopeptides mainly self-assemble *via* β-sheet formation. It was confirmed by FTIR (Fig. 7a and Fig. S12†) in which all the compounds exhibit a main characteristic band centered at 1619–1620 cm^{-1} with an additional one at 1691–1696 cm^{-1}, supporting an anti-parallel β-sheet structure.[78] Interestingly, a broad unresolved absorbance region between 1630 and 1680 cm^{-1} is observed for **PNA(C)-pep**, attributed to a fraction of disordered peptide structures,[79] consistent with the TEM images and the ThT results.

To gain structural insights, circular dichroism was carried out. A clear change in the signal was observed from highly diluted solutions (peptides and nucleopeptides are unstructured at 75 μM and 750 μM, Fig. S13†) to gels. At a high concentration (10 mM, Fig. 7b), **N-pep** and **Aeg-pep** show a minimum at 212–215 nm corresponding to the n–π* electronic transition of the amide groups involved in a β-sheet structure[80] and another negative Cotton effect at ∼200 nm attributed to the π–π* transition of the phenylalanine moieties resulting from aromatic π–π interactions.[81] A close CD signature was obtained for **PNA(G)-pep** with the two minima at 200 nm and 218 nm and a maximum at 189 nm, corresponding to π–π* of the amides, which confirm its structuration *via* β-sheet formation. With **PNA(A)-pep**, the minimum previously observed at 218 nm for the guanine derivative is red-shifted to 233 nm and can reflect more twisted β-sheet assemblies.[82,83] A similar

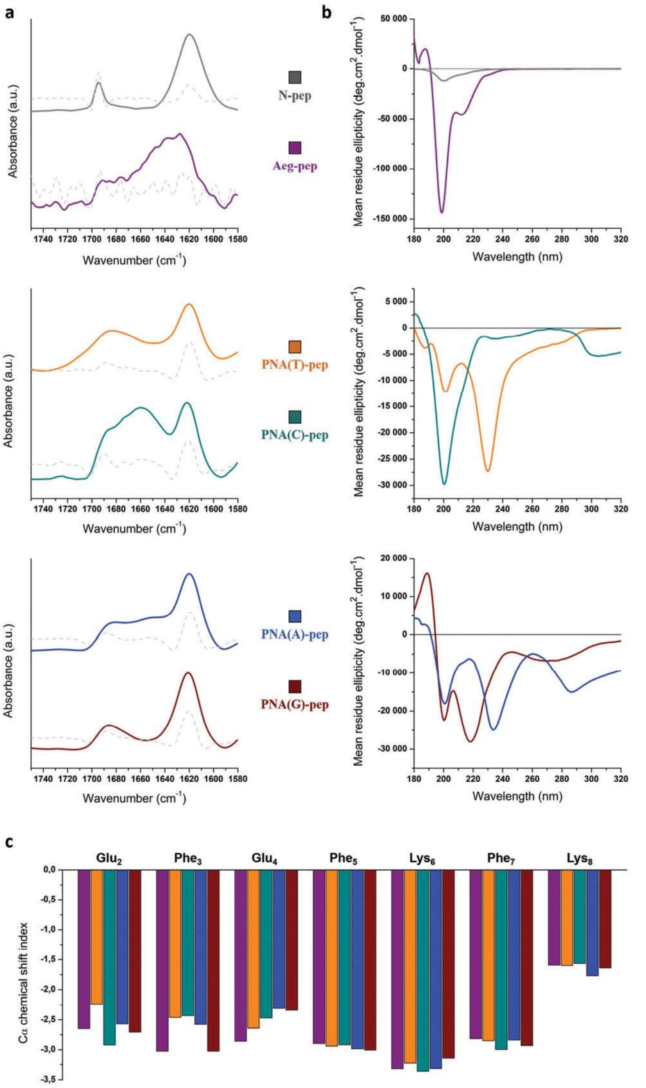

Fig. 7 (a) FTIR spectra of the amide I region for all the samples in their hydrogel state at 15 mM in Tris·HCl (1 M, pH 7.4). The corresponding second derivatives are depicted below each absorbance spectrum (dashed grey). (b) Circular dichroism spectra of all the samples at 10 mM in Tris·HCl (0.67 M, pH 7.4). (c) Chemical shift index of C_α of each amino acid, indicating their involvement in β-sheet structures (in Tris-d$_{11}$·HCl, 0.5 M, pH 7.4).

signature is observed for **PNA(T)-pep**, while **PNA(C)-pep** exhibits a predominant π–π* transition due to π-stacking phenomena, confirming its lower β-sheet-structuration propensity, consistent with the previous results. Interestingly, all the nucleopeptides show an additional negative band above 250 nm, corresponding to the nucleobase chromophores and reflecting a certain degree of pre-organization of the nucleobases in the assembly.[84] Indeed, achiral PNA do not have significant CD signal in the nucleobase region (>240 nm) if they are not in interactions,[85] as observed under diluted conditions (Fig. S13†), confirming the contribution of the nucleobases to the global structuration, *via* hydrogen bonding and/or π-stacking interactions. As a complement to FTIR and ThT, CD experiments reflect for all the compounds a main structuration *via* β-sheet formation, even if at the molecular scale, the thin organization is slightly different, depending on the nature of the nucleobase.

To go further in the understanding of the self-assembly and to evaluate the involvement of each amino acid, we performed the NMR ^{13}C chemical-shift index (also termed CSI) method. This commonly used NMR technique allows the identification of secondary structures of proteins comparing the obtained chemical shifts with the ones referenced for the random coil state.[86,87] As depicted in Fig. 7c, all the amino acid residues have a negative C_α shift difference, confirming the β-strand structuration for all the samples. However, even if the shifts are more similar for amino acids close to the C-term (*i.e.*, –FKFK part) than for the ones close to the N-term (*i.e.*, –EFE– part), the peptide is too short to consider the real differences between each compound (especially because of the NMR time scale), and no clear differentiation can be made, indicating analogous organizations at the molecular level. These data also support that the nucleobases do not interfere directly with the peptide part, suggesting specific nucleobase/nucleobase interactions. Indeed, nucleobases can interact with each other *via* H-bonds (thanks to their Watson–Crick or Hoogsteen faces).[88,89] However, in our case, no characteristic hydrogen bond signals were observed by NMR (*data not shown*), and relaxometry experiments have indicated that the N–H protons of nucleobases are not engaged by hydrogen bonds (*vide supra*). These observations discard the hypothesis of nucleobase/nucleobase interactions *via* hydrogen bonds in the self-assembly. We therefore envisaged that nucleobase stacking plays a pivotal role in the global stability of the nucleopeptide self-assemblies, as occurring in natural DNA and RNA architectures. Computational studies using molecular dynamics[90,91] or hybrid DFT[92] methods highlight stronger self-stacking for purines than for pyrimidines, with stacking free energies $\Delta G_{\text{stack}}\ (G/G) = -1.65\ \text{kcal mol}^{-1} > \Delta G_{\text{stack}}\ (A/A) = -0.89\ \text{kcal mol}^{-1} > \Delta G_{\text{stack}}\ (T/T) = -0.57\ \text{kcal mol}^{-1} > \Delta G_{\text{stack}}\ (C/C) = -0.00\ \text{kcal mol}^{-1}$ (calculated from dinucleoside-monophosphates in a water box),[90] supporting the results and the hierarchy between nucleopeptides, as previously discussed.

To demonstrate the presence of such π-stacking interactions in our systems, fluorescence spectroscopy was selected as a method of choice. All the compounds show a main peak centered in the 400–420 nm range in their emission spectra (Fig. 8a). For **N-pep** and **Aeg-pep**, this peak originates from λ_{ex} = 346 nm and 356 nm (Fig. 8a, black lines), respectively, attributed to the exciton exchange between phenylalanine rings in intermolecular π-stacking interactions.[93,94] In the case of the four nucleopeptides, an additional excitation peak is observed at λ_{ex} = 302 nm to 308 nm (Fig. 8a, red lines), exacerbated at lower emission wavelengths (λ_{em} = 365–375 nm), and absent for **N-pep** and **Aeg-pep**. This characteristic fluorescence has recently been reported for stacking associations of nucleic acids in water,[29] therefore confirming that in our systems nucleobases are mainly involved in the self-assembly process through π-stacking interactions.

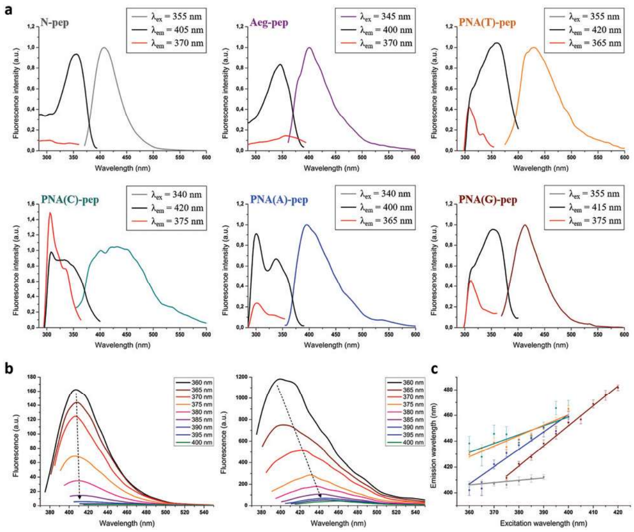

Fig. 8 (a) Fluorescence emission and excitation spectra for all the hydrogels exhibiting the main emission peak with a maximum emission in the 400–420 nm range, and corresponding excitation peaks around 346–356 nm (in black) attributed to Phe/Phe interactions and, for **PNA(X)-pep** (X = **T**, **C**, **A**, and **G**), an additional excitation peak at 302–308 nm (in red) attributed to nucleobase/nucleobase interactions.[29] (b) Evolution of the fluorescence emission spectra at different excitation wavelengths, and (c) corresponding plot of the linear correlation between emission and excitation wavelengths, exhibiting a red-edge excitation shift (REES) for all the four nucleopeptides **PNA(X)-pep** (X = **T**, **C**, **A**, and **G**).

Interestingly, **PNA(X)-pep** (**X** = **T**, **C**, **A**, and **G**) feature a red-edge excitation shift (REES) phenomenon between λ_{ex} = 360 nm to 420 nm and λ_{em} = 400 nm to 480 nm (Fig. 8b and Fig. S14a†), previously described in the literature for several nucleic acid derivatives.[29,95] Briefly, although the fluorescence emission of a fluorophore is independent of the excitation wavelength in dilute solution, a REES effect can be observed in constrained or highly ordered environments, caused by a slow-down of the solvent relaxation time.[96,97] Thus, REES can be considered as an indicator of the dynamics of the fluorophore environment. As depicted in Fig. 8c (and Fig. S14b†), the linear regression slope is the highest for **PNA(G)-pep**, followed by **PNA(A)-pep** > **PNA(T)-pep** > **PNA(C)-pep**, originating from a more constrained environment for the guanine-derivative than for the others, in accordance with the better stacking abilities for the former than for the latter ones, and consistent with the data obtained in NMR relaxometry (*vide supra*). Thus, the modification of the native **N-pep**, for which no significant REES was observed, with the incorporation of one nucleobase induces new REES fluorescent properties adjustable according to the nature of the nucleobase.

Conclusions

In summary, we reported herein on the impact of the incorporation of a peptide nucleic acid (PNA) moiety on the peptide self-assembly processes, from the molecular to the macroscopic scale. Indeed, depending on the nature of the nucleobase (*i.e.*, T, C, A, and G), the mechanical properties of the resulting hydrogel can be substantially modulated with, as observed, a drastic improvement in the gel stiffness by a factor of up to 70 (placing **PNA(G)-pep** among the stiffest peptide-based hydrogels reported so far),[11,50,53,54,56] and a better resistance to external stress, up to 40-fold. Scarcely reported with peptide derivatives,[58,60] the presence of a nucleobase also impacts the thermal behaviors, turning the materials into fully reversible hydrogels able to undergo numerous heating/cooling cycles without loss of their mechanical properties. Such macroscopic modifications originate from mesoscopic (μm and nm range) structural differences as observed by NMR relaxometry and TEM images: compared to native peptides (*i.e.*, **N-pep** and **Aeg-pep**), the newly developed nucleopeptides **PNA(X)-pep** (**X** = **T**, **C**, **A**, and **G**) preferentially form thinner fibers but denser fibrillar networks with an increased number of entanglements, modifying the population of constrained and free water embedded into the hydrogel. Based on thioflavin T assays, we also demonstrate very distinct kinetic properties of fibril formation, mainly composed of β-sheet arrangements at the (supra)molecular level (confirmed by CD and FTIR). Interestingly, although the involvement of each amino acid in the assembly process is similar (NMR CSI experiments), the main differences observed for the nucleopeptides are attributed to their stacking abilities, confirming the trend observed all along this multiscale analysis in which **PNA(G)-pep** > **PNA(A)-pep** > **PNA(T)-pep** > **PNA(C)-pep**. Such specific interactions bring peculiar fluorescence properties to the nucleopeptide-based hydrogels which exhibit uncommon red-edge excitation shift (REES). Altogether, the results discussed herein highlight the ability of peptide nucleic acids (PNA) to modulate and fine-tune the mechanical and physicochemical properties of the peptide-based hydrogels, depending on the nature of the chosen nucleobase. This approach provides new opportunities to adapt and fit hydrogel properties to the intended applications, highlighting the use of biologically inspired chemical moieties, *i.e.*, nucleobases. The presence of nucleobases in PNA-containing peptide-based hydrogels is an opportunity that can be harnessed for the future development of innovative nano- and bio-technological applications such as biosensing and drug delivery,[98,99] sequestration of nucleobase-containing biomolecules with antitumoral applications,[31] stimuli-responsive materials[100] or organic optical devices (based on their REES properties).[95] Thanks to its multiscale approach, this work contributes to the understanding and further development of emerging[28] and highly promising nucleopeptide-based hydrogels.

Materials and methods

Peptide synthesis, purification, and chemical analyses

The peptides were synthesized at a 400 μmol-scale both manually and using an automated ResPep XL synthesizer (Intavis

AG) using a Fmoc/^{t}Bu strategy and double couplings for each amino acid. Preloaded Wang-resin (0.70 mmol g^{-1}, 200–400 mesh) was used. The standard experimental conditions for each coupling were: Fmoc-amino acid (6 equivalents), 2-(1*H*-benzotriazol-1-yl)-1,1,3,3-tetramethyl-uronium tetrafluoroborate (HBTU, 5 equivalents), and 4-methylmorpholine (NMM, 10 equivalents) in dimethylformamide (DMF) and *N*-methyl-2-pyrrolidone (NMP), coupling time = 40 minutes. Fmoc-PNA-G(Bhoc)-OH, PNA-A(Bhoc)-OH, Fmoc-PNA-C(Bhoc)-OH, Fmoc-PNA-T-OH and Fmoc-Aeg(Boc)-OH were introduced manually (3.0 equiv.) using HBTU (3.0 equiv.), and NMM (6.0 equiv.) in DMF and NMP (double coupling, 3 hours, room temperature, 500 rpm). Fmoc-deprotection steps were carried out using a 20% piperidine solution in DMF (3 × 15 min), and final cleavages were achieved using a trifluoroacetic acid/triisopropylsilane/water (92.5/5/2.5) mixture (2 hours). The crude peptides were precipitated from cold diethylether (−20 °C), centrifuged (3 × 5000 rpm, 5 min) washed with cold diethylether, dried under reduced pressure, resolubilized in water and finally, lyophilized. Then, the peptides were dissolved in a solvent A/solvent B (75/25) mixture, sonicated, and purified by semi-preparative HPLC equipped with a Nucleosil (Macherey-Nagel) 100–5 C_{18} 250 × 21 mm column using solvent A (95% water, 5% acetonitrile, 0.1% trifluoracetic acid) and solvent B (100% acetonitrile and 0.1% trifluoroacetic acid) with a 16 min linear gradient (0% to 40% solvent B), followed by 10 min isocratic elution (40% B) and a 14 min linear gradient (up to 100% B) with UV detection at 214 nm. The resulting solutions were evaporated under reduced-pressure and double-lyophilized.

The purity of each peptide was evaluated by analytical reversed-phase HPLC equipped with a Nucleosil (Macherey-Nagel) 100–5 C_{18} 250 × 4.6 mm column using solvent A′ (95% water, 5% acetonitrile, and 0.1% formic acid) and solvent B′ (100% acetonitrile and 0.1% formic acid) with 15 min isocratic elution (100% A′) followed by a 15 min linear gradient (0% to 60% solvent B′) and a 5 min linear gradient (60% to 100% B′) with UV detection at 214 nm. High resolution ESI-MS analyses were performed using a Bruker Daltonics MicrOTOFQ mass spectrometer, and all the compounds were fully characterized by NMR ^{1}H, TOCSY, COSY, ROESY, and NOESY performed using a Bruker Avance III 600 MHz instrument in DMSO-d_6 and analyzed using TOPSPIN and Sparky software.

Sample preparation

As a global procedure, the samples were prepared at 15 mM by dissolving each peptide or nucleopeptide in Tris·HCl (1 M, pH 7.4), deuterated Tris-d_{11}·HCl (1 M, pH 7.4), NaF aqueous solution (1 M, pH 7.4) or DMSO. All the buffers were prepared in deionized water (18.2 MΩ cm). The glass vials containing the solutions were sealed and subsequently heated (heatgun, 5 min, 70 °C), allowing complete dissolution of the starting powder. The samples were used directly (rheology and thioflavin T fluorescence experiments) or stored for 24 hours at room temperature before analysis.

Rheological characterization studies

Dynamic rheological measurements were performed using an AR2000 rheometer (TA Instruments) operating in oscillatory mode, equipped with a Peltier plate temperature control and a Couette geometry immersed inside the samples (see the ESI†). Time sweep experiments were carried out at constant shearing strain using a 0.5% strain amplitude and a 1 rad s^{-1} angular frequency during 360 min, at 20 °C. Frequency sweep experiments were conducted at constant shearing strain using a 0.5% strain amplitude in the range of 0.1–100 rad s^{-1}, at 20 °C. Stress sweep experiments were performed in the range of 0.46–1000 Pa applied stress at a 1 rad s^{-1} angular frequency, at 20 °C. Temperature sweep experiments were carried out at constant shearing strain using a 0.5% strain amplitude, a 1 rad s^{-1} angular frequency and a 1 °C min^{-1} temperature gradient in the range of 20 °C–85 °C. Thermal recovery experiments were conducted at constant shearing strain using a 0.5% strain amplitude, a 1 rad s^{-1} angular frequency applying five heating/cooling cycles. During each cycle, after a one-hour stabilization step at 20 °C, the samples were heated up at 10 °C min^{-1} to reach 85 °C, followed by a 5 min stabilization time (in which no shear was applied). Then, the samples were cooled at 5 °C min^{-1} to reach 20 °C. The storage (G') and loss (G'') moduli reported were chosen at the end of each stabilization step. For thixotropy experiments, the samples were first measured for one hour at 0.5% strain amplitude, and then, five cycles alternating a 5 min period at high strain amplitude (200%) to break the hydrogel followed by a 30 min resting time at 0.5% strain amplitude were applied. All the measurements were repeated for a minimum of three times.

Relaxometry

The ^{1}H NMR relaxometry experiments were performed with a Stelar SMARtracer fast-field-cycling relaxometer (Stelar company, Medde, Italy) in the 5 kHz–10 MHz Larmor frequency range, at 25 °C in 5 mm NMR tubes. For all R_1 measurements, magnetization recovery curves were found to be monoexponential within the experimental errors. 32 different values of the static magnetic field were sampled, with a fixed acquisition field of 7.2 MHz (^{1}H Larmor frequency). Pre-polarized measurements were done between 5 kHz and 4 MHz with a polarization duration varying between 0.7 and 1.5 s, depending on the sample, and at a ^{1}H frequency of 8 MHz, and non-polarized sequence was used between 4 MHz and 10 MHz. Field-switching time was 3 ms. For each B_0 value, R_1 measurements were obtained from the magnetization monoexponential evolution as a function of the time, sampled with 16 values between 0.01 and 4 times the longitudinal relaxation time. 16 accumulations were used for all measurements and a recycle delay of 8 s was applied. Additional measurements were done in the 0.25–10 MHz Larmor frequency range for PNA(G)-pep and PNA(T)-pep. 32 different values of the static magnetic field were sampled in this range and 32 accumulations were used with a recycle delay of 8 s.

Transmission electron microscopy

Transmittance Electron Microscopy (TEM) experiments were performed using a Philips CM200 electron microscope operating at 200 kV and fitted with a CCD MSC 600 Gatan camera. The samples were prepared by placing a drop of each sample (1.5 mM in 100 mM Tris·HCl, pH 7.4) on 200-mesh carbon-coated copper grids (CF-200-Cu-50) for 3 min. Then, excess fluid was removed by capillary action, and a drop of phosphotungstic contrasting agent (2% w/w in deionized water (18.2 MΩ cm)) was deposited for 1 min. The excess was subsequently removed, and the grid was air-dried for 5 min before analysis. Collected data were analysed using Gatan DigitalMicrograph and Fiji software.

Thioflavin T fluorescence

Stock solutions of thioflavin T (750 μM) were prepared in deionized water (18.2 MΩ cm), and the actual concentration was determined through UV-vis spectral analysis at 412 nm with the molar extinction coefficient $\varepsilon_{412\ \text{nm}} = 36\,000\ \text{M}^{-1}\ \text{cm}^{-1}$.[71] The samples were prepared by mixing the ThT solution with peptide solutions (previously dissolved in Tris·HCl (1 M, pH 7.4)) to reach final concentrations [ThT] = 100 μM and [peptide] or [nucleopeptide] = 5 mM. They were subsequently transferred into black 96-well microplates (150 μL per well), protected with an optical adhesive film to avoid evaporation and the fluorescence (λ_{ex} = 440 nm, λ_{em} = 485 nm, response = 1 s, excitation/emission bandwidth = 6 nm, sensitivity PMT = 800 or 1100 V, temperature = 25 °C) was measured during 1000 min (1 point for each 5 minutes, orbital shacking (3 mm, 5 Hz)) with a Xenius SAFAS. Fluorescence emission at 485 nm was plotted as a function of time, and the results are the mean of three to four experiments. Data were fitted using a sigmoidal growth model.[101] Characteristic values were extracted from the graphs: the lag time t_{lag} and t_{50} corresponding to the time required to reach 5% and 50% of the maximum fluorescence intensity, respectively, and the apparent growth rate k_{app} calculated from the tangent at the inflexion point t_{50}.

FTIR

FT-IR measurements were carried out at room temperature using a Tensor27 spectrometer (Bruker) set to ATR mode, in the range of 4000–900 cm^{-1} with a 2 cm^{-1}-resolution. Peptides and nucleopeptides were analyzed as crude powders, as 15 mM solutions in DMSO and as hydrogels in Tris·HCl buffer (see the above-mentioned preparation protocol). Infrared spectra were recorded after a week and represent an average of 256 scans recorded in a single-beam mode and corrected for the background. Data were analyzed, smoothed (Savitzky–Golay, 2nd order, 9 points), and treated using the OPUS software and OriginPro 8.5.

Circular dichroism

Circular dichroism spectra were recorded using a Chirascan Plus spectrophotometer (Applied Photophysics) at 20 °C. Diluted solutions were prepared by dissolving powders in an aqueous solution of NaF (5 mM in deionized water (18.2 MΩ cm) adjusted to pH = 7.4 with NaOH) to a nominal concentration [peptide] or [nucleopeptide] = 75 μM, or in an aqueous solution of NaF (50 mM in deionized water (18.2 MΩ cm) adjusted to pH = 7.4 with NaOH) to a nominal concentration [peptide] or [nucleopeptide] = 750 μM. Their spectra were recorded between 180 and 350 nm (step = 1 nm, response = 0.5 s, bandwidth = 1 nm) averaged on three repetitions in a 1 mm-pathlength cuvette. The hydrogels were prepared in an aqueous solution of NaF (667 mM in deionized water (18.2 MΩ cm) adjusted to pH = 7.4 with NaOH) to a nominal concentration [peptide] or [nucleopeptide] = 10 mM following the preparation protocol. After two days, gels were deposited carefully inside a 0.01 nm-pathlength dismountable cuvette prior to be analyzed. Their spectra were recorded between 180 and 320 nm (step = 0.5 nm, response = 0.5 s, bandwidth = 1 nm) averaged on three repetitions. After background subtraction and smoothing (Savitzky–Golay, 2nd order, 9 points), all raw data (θ, mdeg) were converted into mean residual ellipticity (MRE) according to the equation below:

$$\text{MRE} = \frac{\theta}{(n-1) \times c \times d \times 10}$$

where MRE is in °cm^2 dmol^{-1}, d is the cuvette pathlength in cm, and c is the molar concentration in mol L^{-1}.

NMR CSI

Peptide and nucleopeptide solutions at 5 mM were prepared by dissolving the lyophilized powders in a solution of deuterated Tris-d$_{11}$·HCl (0.5 M, pH 7.4) and 5% D_2O, shaken at 70 °C during 3 min. After one night, the samples are homogenized again by heating at 70 °C and transferred into 5 mm-NMR tubes. The samples are then analyzed by NMR (^{1}H, COSY, NOESY, HSQC and HSQC-TOCSY) using a Bruker Avance III 400 MHz instrument and chemical shifts are obtained using TOPSPIN and Sparky software. The chemical shift index method is applied based on the literature data.[86,87] Due to solubility issues, no exploitable NMR signals are obtained for N-pep, even under more diluted conditions.

Fluorescence

Fluorescence assays were conducted using a FP-8300 spectrofluorometer (JASCO Corp.) on 5 mM samples in Tris·HCl buffer (1 M, pH 7.4). For each experiment, 700 μL of the samples were transferred into quartz cuvettes (1 cm-pathlength). Fluorescence spectra were recorded at 20 °C with a 3D measurement mode: excitation spectra were recorded from 250 to 400 nm (step = 2 nm) for an emission wavelength varying from 265 to 600 nm (step = 5 nm), and emission spectra were recorded from 265 nm to 600 nm (step = 1 nm) for an excitation wavelength varying from 250 to 400 nm (step = 5 nm). Scanning speed was set to 200 nm min^{-1}, response time to 1 s, emission bandwidth to 5 nm and excitation bandwidth to 1 nm. Data were processed and smoothed (Savitzky–Golay, 2nd order, 9 points) using OriginPro 8.5. The maximum of emission for the considered transition is spotted on each smoothed emission spectrum for all compounds when relevant. The associate wavelength is noted in order to draw a $\lambda_{ex}/\lambda_{em}$ plot. REES phenomenon is highlighted by a linear regression on concerned points.

Conflicts of interest

There are no conflicts to declare.

Acknowledgements

L. S. and M. C. A. P. thank the Centre National de la Recherche Scientifique (CNRS) for funding, and T. G. thanks the Ministère de l'Enseignement Supérieur, de la Recherche et de l'Innovation (MESRI) for its Ph.D. grant. The authors would like to thank Anne Robert, Dr Sylvie Fournel-Gigleux and Dr Sandrine Gulberti for allowing access to the Xenius SAFAS fluorimeter, Mathilde Achard and Oliver Fabre for technical support, and the NMR facilities: Plateforme de RMN de l'Institut Jean Barriol (Université de Lorraine, Dr Sébastien Leclerc) and UMS2008 IBSLor (Université de Lorraine, CNRS, INSERM, Dr Marc Quinternet).

References

1 B. J. G. E. Pieters, M. B. Van Eldijk, R. J. M. Nolte and J. Mecinović, *Chem. Soc. Rev.*, 2016, **45**, 24–39.
2 J. J. McManus, P. Charbonneau, E. Zaccarelli and N. Asherie, *Curr. Opin. Colloid Interface Sci.*, 2016, **22**, 73–79.
3 M. Jucker and L. C. Walker, *Nat. Neurosci.*, 2018, **21**, 1341–1349.
4 U. M. Migas, M. K. Quinn and J. J. McManus, *Integr. Biol.*, 2017, **9**, 444–450.
5 J. I. Clark, *Philos. Trans. R. Soc., B*, 2013, **368**, 1–7.
6 S. Yuditskaya, A. F. Suffredini and G. J. Kato, *Expert Rev. Proteomics*, 2010, **7**, 833–848.
7 D. Papapostolou and S. Howorka, *Mol. Biosyst.*, 2009, **5**, 723–732.
8 I. W. Hamley, *Biomacromolecules*, 2019, **20**, 1829–1848.
9 Y. Bai, Q. Luo and J. Liu, *Chem. Soc. Rev.*, 2016, **45**, 2756–2767.
10 D. Mandal, A. Nasrolahi Shirazi and K. Parang, *Org. Biomol. Chem.*, 2014, **12**, 3544–3561.
11 L. M. De Leon Rodriguez, Y. Hemar, J. Cornish and M. A. Brimble, *Chem. Soc. Rev.*, 2016, **45**, 4797–4824.
12 L. Adler-Abramovich and E. Gazit, *Chem. Soc. Rev.*, 2014, **43**, 6881–6893.
13 K. Sato, M. P. Hendricks, L. C. Palmer and S. I. Stupp, *Chem. Soc. Rev.*, 2018, **47**, 7539–7551.
14 J. Li, R. Xing, S. Bai and X. Yan, *Soft Matter*, 2019, **15**, 1704–1715.
15 L. Stefan, in *Amino Acid - New Insights and Roles in Plant and Animal*, ed. T. Asao and M. Asaduzzaman, IntechOpen, 2017, pp. 31–73.
16 M. Kaushik, S. Kaushik, K. Roy, A. Singh, S. Mahendru, M. Kumar, S. Chaudhary, S. Ahmed and S. Kukreti, *Biochem. Biophys. Rep.*, 2016, **5**, 388–395.
17 A. Ghosh and M. Bansal, *Acta Crystallogr., Sect. D: Biol. Crystallogr.*, 2003, **59**, 620–626.
18 F. Pu, J. Ren and X. Qu, *Chem. Soc. Rev.*, 2018, **47**, 1285–1306.
19 N. C. Seeman and H. F. Sleiman, *Nat. Rev. Mater.*, 2017, **3**, 17068.
20 L. Stefan and D. Monchaud, *Nat. Rev. Chem.*, 2019, **3**, 650–668.
21 Y. Shao, H. Jia, T. Cao and D. Liu, *Acc. Chem. Res.*, 2017, **50**, 659–668.
22 M. W. Hentze, A. Castello, T. Schwarzl and T. Preiss, *Nat. Rev. Mol. Cell Biol.*, 2018, **19**, 327–341.
23 W. H. Hudson and E. A. Ortlund, *Nat. Rev. Mol. Cell Biol.*, 2014, **15**, 749–760.
24 Y. F. Drygin, *Nucleic Acids Res.*, 1998, **26**, 4791–4796.
25 N. Sjakste, K. Bielskiene, L. Bagdoniene, D. Labeikyte, A. Gutcaits, Y. Vassetzky and T. Sjakste, *Gene*, 2012, **492**, 54–64.
26 N. Y. Tretyakova, A. Groehler and S. Ji, *Acc. Chem. Res.*, 2015, **48**, 1631–1644.
27 K. Zhou, J. Dong, Y. Zhou, J. Dong, M. Wang and Q. Wang, *Small*, 2019, **15**, 1804044.
28 T. MacCulloch, A. Buchberger and N. Stephanopoulos, *Org. Biomol. Chem.*, 2019, **17**, 1668–1682.
29 C. Avitabile, C. Diaferia, V. Roviello, D. Altamura, C. Giannini, L. Vitagliano, A. Accardo and A. Romanelli, *Chem. – Eur. J.*, 2019, **25**, 14850–14857.
30 M. L. Daly, Y. Gao and R. Freeman, *Bioconjugate Chem.*, 2019, **30**, 1864–1869.
31 H. Wang, Z. Feng, Y. Qin, J. Wang and B. Xu, *Angew. Chem., Int. Ed.*, 2018, **57**, 4931–4935.
32 X. Li, Y. Kuang, H. C. Lin, Y. Gao, J. Shi and B. Xu, *Angew. Chem., Int. Ed.*, 2011, **50**, 9365–9369.
33 X. Du, J. Zhou, X. Li and B. Xu, *Interface Focus*, 2017, **7**, 20160116.
34 D. Yuan, X. Du, J. Shi, N. Zhou, J. Zhou and B. Xu, *Angew. Chem., Int. Ed.*, 2015, **54**, 5705–5708.
35 X. Li, X. Du, Y. Gao, J. Shi, Y. Kuang and B. Xu, *Soft Matter*, 2012, **8**, 7402–7407.
36 D. Yuan, X. Du, J. Shi, N. Zhou, A. A. Baoum, K. O. Al Footy, K. O. Badahdah and B. Xu, *Beilstein J. Org. Chem.*, 2015, **11**, 1352–1359.
37 J. T. M. DiMaio, T. M. Doran, D. M. Ryan, D. M. Raymond and B. L. Nilsson, *Biomacromolecules*, 2017, **18**, 3591–3599.
38 R. Freeman, M. Han, Z. Álvarez, J. A. Lewis, J. R. Wester, N. Stephanopoulos, M. T. McClendon, C. Lynsky, J. M. Godbe, H. Sangji, E. Luijten and S. I. Stupp, *Science*, 2018, **362**, 808–813.
39 D. Wu, J. Zhou, J. Shi, X. Du and B. Xu, *Chem. Commun.*, 2014, **50**, 1992–1994.
40 D. Bonifazi, L. E. Carloni, V. Corvaglia and A. Delforge, *Artif. DNA PNA XNA*, 2012, **3**, 112–122.

41 E. Quijano, R. Bahal, A. Ricciardi, W. M. Saltzman and P. M. Glazer, *Yale J. Biol. Med.*, 2017, **90**, 583–598.

42 A. Mohammed, A. F. Miller and A. Saiani, *Macromol. Symp.*, 2007, **251**, 88–95.

43 J. Gao, C. Tang, M. A. Elsawy, A. M. Smith, A. F. Miller and A. Saiani, *Biomacromolecules*, 2017, **18**, 826–834.

44 C. Tang, A. F. Miller and A. Saiani, *Int. J. Pharm.*, 2014, **465**, 427–435.

45 L. Szkolar, J. B. Guilbaud, A. F. Miller, J. E. Gough and A. Saiani, *J. Pept. Sci.*, 2014, **20**, 578–584.

46 S. Wan, S. Borland, S. M. Richardson, C. L. R. Merry, A. Saiani and J. E. Gough, *Acta Biomater.*, 2016, **46**, 29–40.

47 L. A. Castillo Diaz, M. Elsawy, A. Saiani, J. E. Gough and A. F. Miller, *J. Tissue Eng.*, 2016, **7**, 1–15.

48 L. Li, J. Li, J. Guo, H. Zhang, X. Zhang, C. Yin, L. Wang, Y. Zhu and Q. Yao, *Adv. Funct. Mater.*, 2019, **29**, 1807356.

49 R. G. Weiss and P. Terech, in *Molecular gels: Materials with self-assembled fibrillar networks*, ed. R. G. Weiss and P. Terech, Springer, 2006, ch. 8, pp. 241–252.

50 A. Bertolani, L. Pirrie, L. Stefan, N. Houbenov, J. S. Haataja, L. Catalano, G. Terraneo, G. Giancane, L. Valli, R. Milani, O. Ikkala, G. Resnati and P. Metrangolo, *Nat. Commun.*, 2015, **6**, 7574.

51 M. C. Cringoli, S. Kralj, M. Kurbasic, M. Urban and S. Marchesan, *Beilstein J. Nanotechnol.*, 2017, **8**, 1553–1562.

52 J. Rubio-Magnieto, M. Tena-Solsona, B. Escuder and M. Surin, *RSC Adv.*, 2017, **7**, 9562–9566.

53 S. H. Hiew, H. Mohanram, L. Ning, J. Guo, A. Sánchez-Ferrer, X. Shi, K. Pervushin, Y. Mu, R. Mezzenga and A. Miserez, *Adv. Sci.*, 2019, **6**, 1901173.

54 Y. Loo, A. Lakshmanan, M. Ni, L. L. Toh, S. Wang and C. A. E. Hauser, *Nano Lett.*, 2015, **15**, 6919–6925.

55 S. Boothroyd, A. F. Miller and A. Saiani, *Faraday Discuss.*, 2013, **166**, 195–207.

56 A. Lakshmanan, D. W. Cheong, A. Accardo, E. Di Fabrizio, C. Riekel and C. A. E. Hauser, *Proc. Natl. Acad. Sci. U. S. A.*, 2013, **110**, 519–524.

57 N. Zanna and C. Tomasini, *Gels*, 2017, **3**, 39.

58 C. Liu, Q. Zhang, S. Zhu, H. Liu and J. Chen, *RSC Adv.*, 2019, **9**, 28299–28311.

59 B. Jeong, S. W. Kim and Y. H. Bae, *Adv. Drug Delivery Rev.*, 2012, **64**, 154–162.

60 A. Dasgupta, J. H. Mondal and D. Das, *RSC Adv.*, 2013, **3**, 9117–9149.

61 R. Kimmich and E. Anoardo, *Prog. Nucl. Magn. Reson. Spectrosc.*, 2004, **44**, 257–320.

62 R. Kimmich, in *NMR - Tomography, Diffusometry, Relaxometry*, Springer, ed. R. Kimmich, 1st edn, 1997.

63 D. Kruk, A. Kubica, W. Masierak, A. F. Privalov, M. Wojciechowski and W. Medycki, *Solid State Nucl. Magn. Reson.*, 2011, **40**, 114–120.

64 D. Kruk, E. Masiewicz, A. M. Borkowska, P. Rochowski, P. H. Fries, L. M. Broche and D. J. Lurie, *Biomolecules*, 2019, **9**, 652.

65 E. P. Sunde and B. Halle, *J. Magn. Reson.*, 2010, **203**, 257–273.

66 Y. Liu, L. Zhang and W. Wei, *Int. J. Nanomed.*, 2017, **12**, 659–670.

67 Y. Ding, T. Ji, Y. Zhao, Y. Zhang, X. Zhao, R. Zhao, J. Lang, X. Zhao, J. Shi, S. Sukumar and G. Nie, *Mol. Cancer Ther.*, 2015, **14**, 2390–2400.

68 Q. Zou, L. Zhang, X. Yan, A. Wang, G. Ma, J. Li, H. Möhwald and S. Mann, *Angew. Chem., Int. Ed.*, 2014, **53**, 2366–2370.

69 I. Alfonso, M. Bru, M. Isabel Burguete, E. García-Verdugo and S. V. Luis, *Chem. – Eur. J.*, 2010, **16**, 1246–1255.

70 H. Arakawa, K. Takeda, S. L. Higashi, A. Shibata, Y. Kitamura and M. Ikeda, *Polym. J.*, 2020, DOI: 10.1038/s41428-019-0301-5. Q12

71 M. Groenning, *J. Chem. Biol.*, 2010, **3**, 1–18.

72 C. Xue, T. Y. Lin, D. Chang and Z. Guo, *R. Soc. Open Sci.*, 2017, **4**, 160696.

73 K. Wang, J. D. Keasling and S. J. Muller, *Int. J. Biol. Macromol.*, 2005, **36**, 232–240.

74 S. Marchesan, C. D. Easton, K. E. Styan, L. J. Waddington, F. Kushkaki, L. Goodall, K. M. McLean, J. S. Forsythe and P. G. Hartley, *Nanoscale*, 2014, **6**, 5172–5180.

75 A. Z. Cardoso, A. E. Alvarez Alvarez, B. N. Cattoz, P. C. Griffiths, S. M. King, W. J. Frith and D. J. Adams, *Faraday Discuss.*, 2013, **166**, 101–116.

76 D. M. Ryan, S. B. Anderson and B. L. Nilsson, *Soft Matter*, 2010, **6**, 3220.

77 M. C. Branco, F. Nettesheim, D. J. Pochan, J. P. Schneider and N. J. Wagner, *Biomacromolecules*, 2009, **10**, 1374–1380.

78 R. Sarroukh, E. Goormaghtigh, J. M. Ruysschaert and V. Raussens, *Biochim. Biophys. Acta, Biomembr.*, 2013, **1828**, 2328–2338.

79 L. J. Juszczak, *J. Biol. Chem.*, 2004, **279**, 7395–7404.

80 S. M. Kelly, T. J. Jess and N. C. Price, *Biochim. Biophys. Acta, Proteins Proteomics*, 2005, **1751**, 119–139.

81 C. J. Bowerman and B. L. Nilsson, *J. Am. Chem. Soc.*, 2010, **132**, 9526–9527.

82 C. Lara, N. P. Reynolds, J. T. Berryman, A. Xu, A. Zhang and R. Mezzenga, *J. Am. Chem. Soc.*, 2014, **136**, 4732–4739.

83 A. Iyer, S. J. Roeters, V. Kogan, S. Woutersen, M. M. A. E. Claessens and V. Subramaniam, *J. Am. Chem. Soc.*, 2017, **139**, 15392–15400. Q13

84 R. Corradini, T. Tedeschi, S. Sforza and R. Marchelli, in *Comprehensive Chiroptical Spectroscopy*, ed. N. Berova, P. L. Polavarapu, K. Nakanishi and R. W. Woody, Wiley, 1st edn, 2012, ch. 18, vol. 2, pp. 587–614.

85 T. Koch, M. Naesby, P. Wittung, M. Jørgensen, C. Larsson, O. Buchardt, C. J. Stanley, B. Nordén, P. E. Nielsen and H. Ørum, *Tetrahedron Lett.*, 1995, **36**, 6933–6936.

86 S. P. Mielke and V. V. Krishnan, *Prog. Nucl. Magn. Reson. Spectrosc.*, 2009, **54**, 141–165.

87 D. S. Wishart and B. D. Sykes, *J. Biomol. NMR*, 1994, **4**, 171–180.

88 N. B. Leontis, J. Stombaugh and E. Westhof, *Nucleic Acids Res.*, 2002, **30**, 3497–3531.

89 W. H. Gmeiner and B. J. Walberer, Base pairing in DNA: unusual patterns, in *Encyclopedia of Life Sciences*, 2001, pp. 1–10.

90 R. F. Brown, C. T. Andrews and A. H. Elcock, *J. Chem. Theory Comput.*, 2015, **11**, 2315–2328.

91 R. A. Friedman and B. Honig, *Biophys. J.*, 1995, **69**, 1528–1535.

92 Y. Wang, *J. Phys. Chem. C*, 2008, **112**, 14297–14305.

93 C. Diaferia, V. Roviello, G. Morelli and A. Accardo, *ChemPhysChem*, 2019, **20**, 2774–2782.

94 M. Ziaunys and V. Smirnovas, *PeerJ*, 2019, **7**, e6518.

95 O. Berger, L. Adler-Abramovich, M. Levy-Sakin, A. Grunwald, Y. Liebes-Peer, M. Bachar, L. Buzhansky, E. Mossou, V. T. Forsyth, T. Schwartz, Y. Ebenstein, F. Frolow, L. J. W. Shimon, F. Patolsky and E. Gazit, *Nat. Nanotechnol.*, 2015, **10**, 353–360.

96 A. P. Demchenko, *Luminescence*, 2002, **17**, 19–42.

97 S. Haldar, A. Chaudhuri and A. Chattopadhyay, *J. Phys. Chem. B*, 2011, **115**, 5693–5706.

98 J. Gačanin, C. V. Synatschke and T. Weil, *Adv. Funct. Mater.*, 2020, **30**, 1906253.

99 J. Li, L. Mo, C. H. Lu, T. Fu, H. H. Yang and W. Tan, *Chem. Soc. Rev.*, 2016, **45**, 1410–1431.

100 Y. Yu, B. Jin, Y. Li and Z. Deng, *Chem. – Eur. J.*, 2019, **25**, 9785–9798.

101 P. Arosio, T. P. J. Knowles and S. Linse, *Phys. Chem. Chem. Phys.*, 2015, **17**, 7606–7618.